ACS APPLIED MATERIALS & INTERFACES

Research Article

www.acsami.org

Rational Design of Molecular Hole-Transporting Materials for Perovskite Solar Cells: Direct versus Inverted Device Configurations

Roberto Grisorio,[*,†,‡] Rosabianca Iacobellis,[§,∥] Andrea Listorti,[‡,⊥] Luisa De Marco,[*,‡] Maria Pia Cipolla,[§,∥] Michele Manca,[§] Aurora Rizzo,[‡] Antonio Abate,[*,#,▽] Giuseppe Gigli,[‡,⊥] and Gian Paolo Suranna[†,‡]

[†]DICATECh - Dipartimento di Ingegneria Civile, Ambientale, del Territorio, Edile e di Chimica, Politecnico di Bari, Via Orabona, 4, I-70125 Bari, Italy

[‡]CNR-NANOTEC, Istituto di Nanotecnologia, c/o Campus Ecotekne, Università del Salento, Via Monteroni, 73100 Lecce, Italy

[§]Center for Biomolecular Nanotechnologies (CBN), Fondazione Istituto Italiano di Tecnologia, Via Barsanti 14, 73010, Arnesano, Italy

[∥]Dipartimento di Ingegneria dell'Innovazione, Università del Salento, via per Monteroni, 73100, Lecce, Italy

[⊥]Dipartimento di Matematica e Fisica "E. De Giorgi", Università del Salento, Campus Universitario via Monteroni, 73100 Lecce, Italy

[#]Adolphe Merkle Institute, Chemin des Verdiers 4, CH-1700 Fribourg, Switzerland

[▽]Young Investigator Group Active Materials and Interfaces for Stable Perovskite Solar Cells, Helmholtz-Zentrum Berlin für Materialien und Energie, Kekuléstrasse 5, 12489 Berlin, Germany

Supporting Information

ABSTRACT: Due to a still limited understanding of the reasons making 2,2′,7,7′-tetrakis(*N*,*N*-di-*p*-methoxyphenylamine)-9,9′-spirobifluorene (Spiro-OMeTAD) the state-of-the-art hole-transporting material (HTM) for emerging photovoltaic applications, the molecular tailoring of organic components for perovskite solar cells (PSCs) lacks in solid design criteria. Charge delocalization in radical cationic states can undoubtedly be considered as one of the essential prerequisites for an HTM, but this aspect has been investigated to a relatively minor extent. In marked contrast with the 3-D structure of Spiro-OMeTAD, truxene-based HTMs **Trux1** and **Trux2** have been employed for the first time in PSCs fabricated with a direct (n-i-p) or inverted (p-i-n) architecture, exhibiting a peculiar behavior with respect to the referential HTM. Notwithstanding the efficient hole extraction from the perovskite layer exhibited by **Trux1** and **Trux2** in direct configuration devices, their photovoltaic performances were detrimentally affected by their poor hole transport. Conversely, an outstanding improvement of the photovoltaic performances in dopant-free inverted configuration devices compared to Spiro-OMeTAD was recorded, ascribable to the use of thinner HTM layers. The rationalization of the photovoltaic performances exhibited by different configuration devices discussed in this paper can provide new and unexpected prospects for engineering the interface between the active layer of perovskite-based solar cells and the hole transporters.

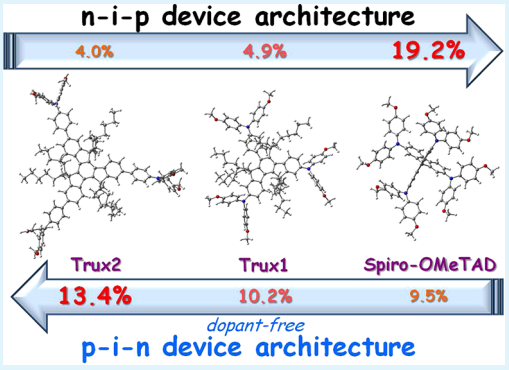

KEYWORDS: *perovskite solar cell, hole-transport materials, p-i-n configuration, electrochemistry, spectroelectrochemistry*

INTRODUCTION

Widely employed in organic light-emitting diodes in the past decades,[1] the renewed interest awakened on π-conjugated arylamines is justified by their use as hole-transporting materials (HTMs) in highly performing perovskite-based solar cells (PSCs).[2,3] In this technology, the perovskite acts as light absorber, while the HTM role consists in the extraction of the photogenerated holes from the perovskite active layer and in their transport to the corresponding electrode.[4−9] The commercially available 2,2′,7,7′-tetrakis(*N*,*N*-di-*p*-methoxyphenylamine)-9,9′-spirobifluorene (Spiro-OMeTAD) represents the state-of-the-art HTM reference for PSCs; however, its synthesis is complex and expensive, the purification process is costly, and its hole conductivity is relatively low. These drawbacks would have a significant impact on low-cost and large-scale photovoltaic applications. Although a conspicuous number of potential candidates[10−19] to replace Spiro-OMeTAD have been recently proposed, most of them did not eventually exhibit satisfactory efficiencies justifying their lengthy synthesis.[20−29] This status is also due to a fundamentally limited

Received: April 19, 2017
Accepted: July 3, 2017
Published: July 3, 2017

DOI: 10.1021/acsami.7b05484
ACS Appl. Mater. Interfaces 2017, 9, 24778−24787

Scheme 1. Chemical Structure and Synthetic Sequence for the Obtainment of Trux1 and Trux2

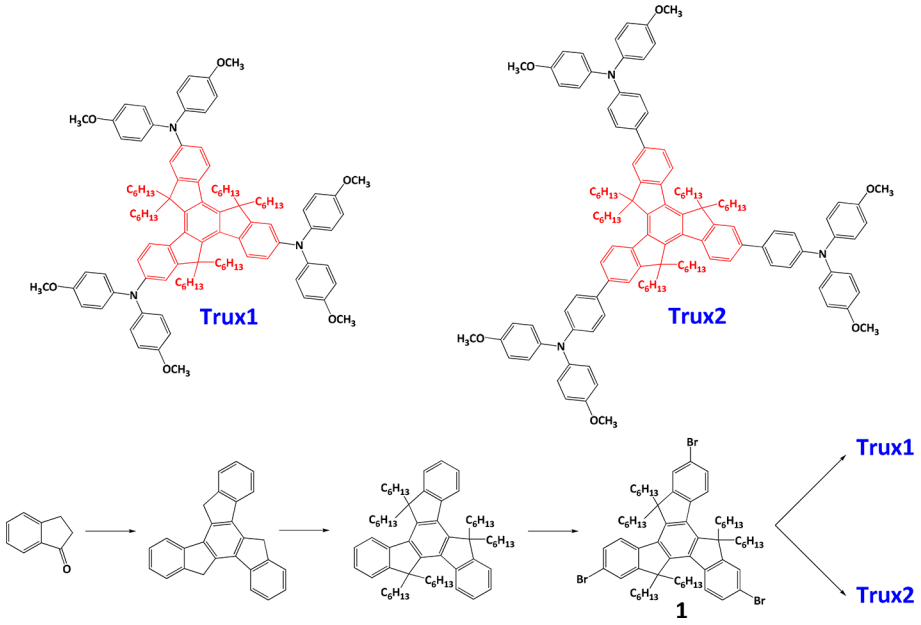

understanding of the key features making Spiro-OMeTAD such an efficient HTM in the device, and therefore to a misjudgment of the criteria needed for the molecular design of high performance alternatives attainable through relatively facile synthesis. At the same time, the research on this topic is complicated by the fact that the mere comparison of HTM efficiency exhibited by devices constructed in different research laboratories might be misleading, since the performance itself depends on several other factors such as the perovskite material/film quality, device geometry, fabrication technologies, test conditions, only to cite the main ones.

Apart from the thermodynamic prerequisite required for hole extraction from the perovskite absorber, the introduction of an adequate number of arylamine groups decorating the HTM scaffold seems to be the sole "*fil rouge*" emerging thus far from the analysis of the relevant literature on PSCs. This structural feature is probably necessary to promote an efficient hole extraction at the perovskite/HTM interface as well as the intermolecular hole hopping during charge drift within the HTM layer. At the same time, since the charge-transport dynamics involves organic molecules in their neutral and radical cation forms, charge or spin distributions within HTM^+ species are also crucial for ensuring efficient hole transport in perovskite solar cells. Surprisingly, no studies have yet been focused on unravelling the implications of the electronic coupling between the redox centers (arylamine groups) belonging to the HTM on the photovoltaic properties in PSCs.

To this purpose, an interesting structural *motif* is represented by truxene, a planar heptacyclic polyarene structure that can be regarded as constituted by three annulated fluorene moieties, which could straightforwardly allocate up to three arylamine groups.[30] The three methylene bridges added to rigidify the structure and to keep the four phenyl rings coplanar, are also prone to be readily functionalized with alkyl chains to warrant suitable solubility to the target molecules. Two truxene-based molecules: **Trux1**[31] and **Trux2**—the latter bearing a phenylene spacer between the truxene core and the three terminal bis(*p*-anisyl)amine groups—were implemented in PSCs, and for the first time, their photovoltaic behavior was investigated in both direct (or n-i-p) and inverted (or p-i-n) configuration devices.[32] The differences between the two architectures mainly rely on the layer (hole- or electron-transporting) used at the device bottom, consequently dictating on which substrate the perovskite grows and which kind of HTM/perovskite interface is formed. The figures of merit exhibited by **Trux1** and **Trux2** compared to Spiro-OMeTAD were drastically affected by the device configuration, due to different organic layer thickness and perovskite/HTM interfaces, highlighting the synergic cooperation between molecular design and solar cell architecture for photovoltaic performance optimization.

RESULTS AND DISCUSSION

Synthesis and Characterization. The truxene building block **1**[33] was synthesized in three steps starting from the condensation of 1-indanone, followed by the introduction of *n*-hexyl chains and subsequent bromination, as shown in Scheme 1.

The target molecule **Trux1** was prepared in 68% yield via a Buchwald−Hartwig C−N cross-coupling between **1** and the commercially available *p*-methoxy-diphenylamine in toluene, using $Pd(AcO)_2$/dppf as the catalyst precursor and *tert*-BuONa as the base. Analogously, the **Trux2** congener was synthesized via a Suzuki−Miyaura C−C cross-coupling between **1** and 4-methoxy-*N*-(4-methoxyphenyl)-*N*-(4-(4,4,5,5-tetramethyl-1,3,2-dioxaborolan-2-yl)phenyl)aniline[34] in the presence of $Pd(PPh_3)_4$ as the catalyst precursor, a 2 M K_2CO_3 aqueous solution acting as the base and toluene as the solvent in 75% yield. The molecular structures of **Trux1** and **Trux2** were confirmed by NMR (Figures S1−S4).

In order to evaluate the stability and thermal behavior of the synthesized materials, thermogravimetric analyses (TGA) and differential scanning calorimetry (DSC) measurements were carried out on both HTMs and on Spiro-OMeTAD for comparison. In the case of **Trux2**, the 5% weight loss (commonly accepted as the event associated with the material decomposition) was observed at 410 °C, slightly lower than the decomposition temperature recorded for Spiro-OMeTAD (424 °C), as shown in Figure 1A. Conversely **Trux1** exhibits a lower

DOI: 10.1021/acsami.7b05484
ACS Appl. Mater. Interfaces 2017, 9, 24778−24787

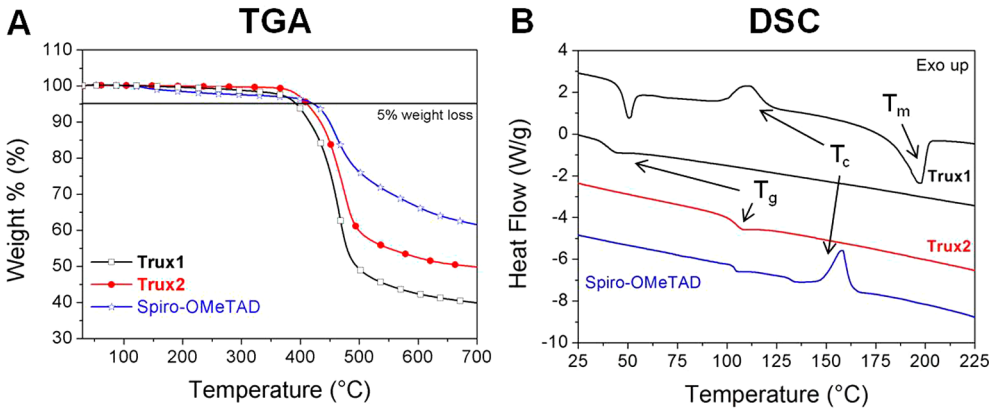

Figure 1. (A) Thermogravimetric curves of **Trux1**, **Trux2**, and Spiro-OMeTAD. (B) Comparison between DSC traces of **Trux1** (first and second heating scans), **Trux2** (second heating scan), and Spiro-OMeTAD (first heating scan), identifying the clear glass transition (T_g), cold crystallization (T_c), and melting (T_m) events.

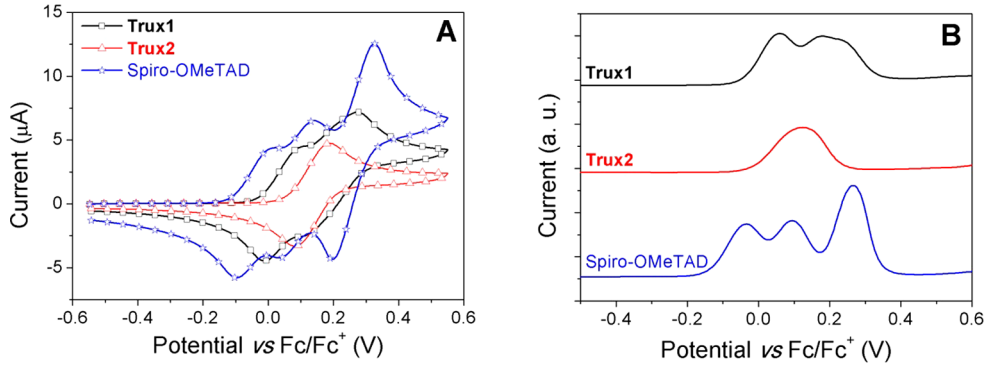

Figure 2. (A) CV traces of **Trux1**, **Trux2**, and Spiro-OMeTAD recorded in methylene chloride (~1.0×10^{-4} M) and (B) the corresponding differential pulse voltammetries.

thermal stability with respect to **Trux2** starting to decompose at 393 °C. Interesting results crop up from the DSC analysis, demonstrating that **Trux2** is a fully amorphous material, only showing a clear glass transition at 106 °C (Figure 1B), suggesting a stabilized amorphous state particularly relevant for photovoltaic applications.[35,36] On the other hand, the thermal behavior of **Trux1** during the first heating scan revealed a glass transition with enthalpic relaxation at 47 °C, followed by a cold crystallization of the amorphous material at 112 °C, leading to sample melting at 197 °C. However, the second heating scan only confirmed the presence of the glass transition at 43 °C, hinting at the amorphous character of **Trux1**. The thermal behavior of **Trux1** during the first heating scan is very similar to the one recorded for Spiro-OMeTAD, which exhibited a glass transition at 104 °C and a cold crystallization of the amorphous material at 158 °C, followed by melting at 247 °C. Conversely, the second heating scan revealed a weak glass transition at 119 °C and a cold crystallization of the amorphous material at 188 °C, followed by melting at 236 °C (Figure S5). This behavior could be due to the formation of a different and more stable crystalline phase following the thermal history erasure of the as-prepared sample.

Electrochemical Characterization. The two or more identical redox centers of organic species placed sufficiently distant from one another to rule out direct overlap between their localized orbitals[37,38] attain different formal oxidation states during electron removal, generating mixed-valence systems, in which the actual electron density at each redox site reflects the degree of charge distribution between the individual redox centers, which, in turn, depends on the presence and nature of the π-spacer.[39] Electronic coupling decreases the difference in intrinsic charge and valence states of the individual redox sites and renders them electronically similar, or even identical. Arylamines constitute useful redox sites for the molecular assembly of organic mixed-valence systems mainly due to their well-defined $N^{+/0}$ processes occurring in a relatively low potential region, as well as to the high extinction coefficients characterizing their intervalence charge-transfer (IVCT) transitions.[40−44] These absorptions originate from intramolecular electron transfer processes consequent to photochemical excitation which lead to a redistribution of the formal redox states within the mixed-valence species and straightforwardly permit to explore the degree of charge distribution between the redox centers.

Electrochemical analysis carried out with cyclic voltammetry (CV) and differential pulse voltammetry (DPV) experiments represents a useful instrument to evaluate the ionization potential of HTMs and the feasibility of hole extraction at the perovskite/HTM interface in PSCs. At the same time, these techniques can also provide important information about electronic coupling between the identical redox centers of the molecule, which is experimentally observed through the potential splitting of the oxidation events involving the formally identical redox centers. The potential splitting is generated by charge distribution in the mixed-valence state of the material after electron(s) removal during voltammetry measurements. In

DOI: 10.1021/acsami.7b05484
ACS Appl. Mater. Interfaces 2017, 9, 24778−24787

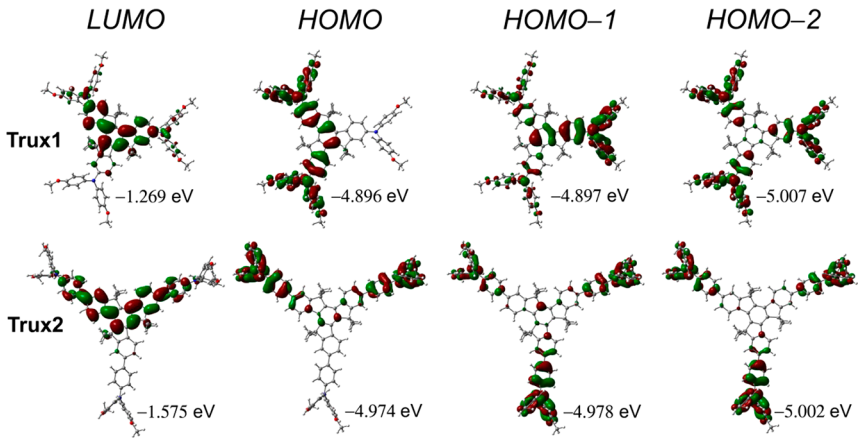

Figure 3. Isodensity plots (0.02 e/bohr^3) of the LUMO, HOMO, HOMO−1, and HOMO−2 for **Trux1** and **Trux2** and the corresponding DFT-calculated energies.

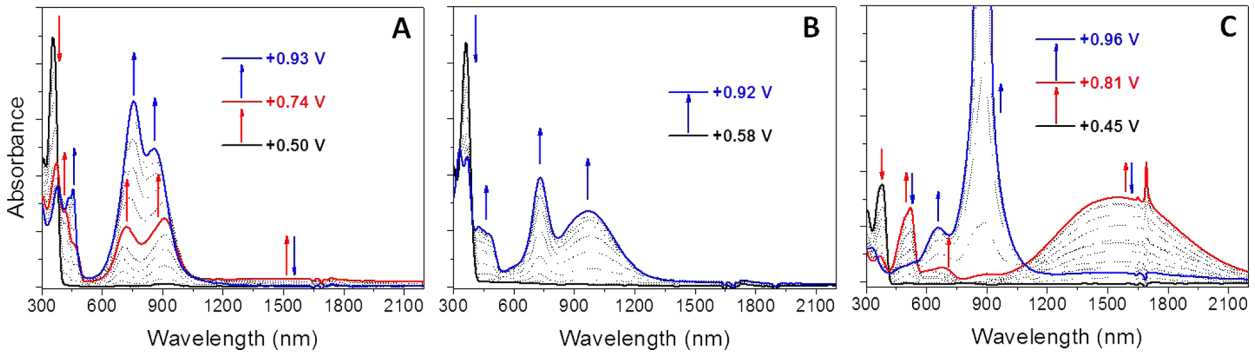

Figure 4. Absorption spectral changes of **Trux1** (A), **Trux2** (B), and Spiro-OMeTAD (C) upon electrochemical oxidation in CH_2Cl_2.

the case of **Trux1**, the CV trace recorded in methylene chloride at low potentials apparently showed two reversible anodic events; by contrast, the oxidation behavior of **Trux2** was characterized by a single reversible event (Figure 2A). For comparison, the CV scan carried out on Spiro-OMeTAD apparently revealed the presence of three electrochemical events in the same potential region under investigation. Further insights carried out by DPV (Figure 2B) confirmed the single oxidation event in the case of **Trux2**, while disclosing three oxidation events in the case of **Trux1**, plausibly owing to electronic coupling between its three redox centers present onto the molecule. In fact, electrons from bis(*p*-anisyl)amine groups are removed at almost identical potentials in the case of **Trux2**, since the structural framework (truxene core *plus* phenylene spacer) that connects the spatially separated actual redox-active sites acts as an insulator, thereby hampering the mesomeric stabilization of the mixed-valence states. Conversely, a strong electronic coupling has to be expected in mixed-valence Spiro-OMeTAD, occurring between the two bis(*p*-anisyl)amine subunits placed onto the same fluorene unit (Figure 2A). However, it appears from CV scans of Spiro-OMeTAD that the first electron removal from the two isolated halves of the molecule results to be electrochemically split into two oxidation events, clearly more evident (−0.04 V and +0.10 V vs Fc/Fc$^+$) in the DPV measurements shown in Figure 2B. This behavior hints that, upon one electron oxidation in Spiro-OMeTAD, the formed positive charge is also mesomerically stabilized by the arylamine subunits present on the opposite half of the molecule (*vide infra*), due to homoconjugation, as recently suggested by Nakamura and co-workers for 3-D carbon-bridged oligophenylenevinylene backbones.[45]

On the basis of the electrochemical data, recorded in solution, the highest-occupied molecular orbitals (HOMOs) of the materials were estimated at −5.15 eV for **Trux1** and at −5.24 eV for **Trux2**, whereas, under the same conditions, Spiro-OMeTAD exhibited a lower (−5.02 eV) oxidation potential. Assuming the valence band edge of mixed-ion perovskite to be at −5.65 eV (vs vacuum),[46] the two truxene-based molecules show enough overpotential to promote charge extraction at the HTM/perovskite interfaces. Moreover, **Trux1** and **Trux2** exhibit an excellent band alignment between the HOMO of the HTM and the valence band edge of the $MAPbI_3$ perovskite. Hence, an efficient hole injection from the HTM to the perovskite is expected.

Within the approximations of Koopman's theorem,[47] the oxidation potential trend well correlates with the results of the DFT calculations (Figure 3 and Figure S6), corroborating the assumption that the HOMO of **Trux2** is substantially stabilized by the introduction of the phenylene spacers. It is worth noting that the lowest-unoccupied molecular orbitals (LUMOs) of **Trux1** and **Trux2** are mainly localized on the truxene core, whereas the electron density of the relevant HOMOs differs significantly. The HOMO of **Trux1** is evidently localized on two triarylamine groups as well as on the corresponding interconnecting portion of the truxene system. Conversely, although substantially similar to the frontier orbital of **Trux1**, the contribution of the π-bridge in the HOMO description in the case of **Trux2** is considerably lower (Figure 3), probably due to the dihedral distortion introduced by the presence of the

DOI: 10.1021/acsami.7b05484
ACS Appl. Mater. Interfaces 2017, 9, 24778−24787

phenylene moiety, hampering effective orbital overlap and therefore conjugation. For these reasons, in the case of **Trux2**, the three frontier orbitals HOMO, HOMO−1, and HOMO−2 are almost degenerate owing to the presence of the three isolated triarylamine subunits, while a calculated energy splitting (0.111 eV) between HOMO and HOMO−2 was observed in the case of **Trux1**.

Spectroelectrochemical Characterization. Although electrochemical measurements and theoretical calculations provide important qualitative information about ground state delocalization of the HTM under study, the electronic coupling between the redox-active subunits present onto the molecules needs to be addressed by spectroelectrochemistry. To investigate the spectroscopic properties of their radical cations, **Trux1** and **Trux2** were subjected to oxidative electrolysis at a platinum grid working electrode (Figures S7−S9). Figure 4 shows the absorption spectral changes of **Trux1** recorded during the oxidative spectroelectrochemical measurements. In the first one-electron oxidation step (single oxidation; the potential was gradually increased from +0.50 to +0.64 V vs Ag/Ag^+), the UV-centered absorption band at 354 nm of the neutral molecule significantly decreased and strong visible/NIR absorptions attributable to $\mathbf{Trux1}^+$ appeared. Guided by DFT and TD-DFT calculations (see Figure S10 and Table S1), these absorptions can be attributed to the following electronic transitions: (i) the bands in the region 400−500 nm to truxene$^+$-localized transitions; (ii) the absorption peaked at 724 nm to N^+-localized transitions; and (iii) the absorption peaked at 937 nm to truxene → N^+ charge transfer transitions. The occurrence of N^+-localized and truxene → N^+ charge transfer transitions suggests that the radical spin is dominated by the bis(*p*-anisyl)amine subunits, although the appearance of truxene$^+$-localized absorptions suggests that the truxene core was also partially oxidized. During the second one-electron oxidation step (potential was gradually increased from +0.64 to +0.74 V vs Ag/Ag^+), the spectral changes followed the same behavior observed for the first oxidation step. The intervalence charge transfer (IVCT) transition was only barely detectable as a broad band (1400−1500 nm, difficult to be peaked) after the formation of $\mathbf{Trux1}^+$ and $\mathbf{Trux1}^{2+}$. The intensity and shape of the IVCT band observed in $\mathbf{Trux1}^+$ and $\mathbf{Trux1}^{2+}$ is typical of class-II mixed valence systems, in which the electronic coupling renders the redox subunits more similar, but still different with respect to their intrinsic electron densities. This means that the charge density, although not uniformly, is distributed along the whole molecule, the hypothesis being as supported by the calculated electron spin density distributions (*vide infra*).

The mesomeric stabilization of the formed charge due to the residual bis(*p*-anisyl)amine subunit is confirmed by the fact that, once $\mathbf{Trux1}^{2+}$ is generated at +0.74 V, the IVCT band promptly disappeared upon further potential increase, owing to the complete oxidation of redox-active groups, as corroborated by theoretical calculations (Figure S11). Proceeding with the oxidation, in fact, new well-defined substructural bands appeared in the region 400−550 nm, while the band at 750 nm associated with the N^+-localized transitions of $\mathbf{Trux1}^{3+}$ relatively increased its intensity with respect to the truxene → N^+ charge transfer transition, which was found blue-shifted (860 nm). To substantiate this behavior and to probe the effective p-doping by the Co(III)-complex FK209 used for PSC device fabrication, the absorption spectral modifications following the chemical oxidation of **Trux1** upon addition of FK209 in dichloromethane were analyzed (Figure S12).

The spectroelectrochemical behavior of **Trux2** revealed that, during the oxidative electrolysis in the range between +0.58 and +0.92 V, the UV-centered absorption band at 363 nm of the neutral molecule significantly decreased and strong visible/NIR absorptions of oxidized **Trux2** appeared (Figure 4B). Differently from what was observed in the case of **Trux1**, however, the spectral changes of **Trux2** occur independently of the potential increment. The insurgent absorptions features associated with the oxidized forms of **Trux2** can, again, schematically be assigned to the following electronic transitions: (i) the bands in the region 400−500 nm to π-bridge$^+$-localized transitions; (ii) the absorption peaked at 733 nm to N^+-localized transitions; and (iii) the absorption peaked at 974 nm to π-bridge → N^+ charge transfer transitions (Figure S10 and Table S2). Also in this case, the occurrence of N^+-localized and π-bridge → N^+ charge transfer transitions suggests that the electron spin density is dominated by the bis(*p*-anisyl)amine subunits, although the appearance of π-bridge$^+$-localized absorptions suggests that the truxene-based core was also partially oxidized. Since no IVCT bands were observed during oxidation of **Trux2**, it can be supposed that the three arylamine redox centers are not interacting in the molecule, justifying the absence of potential splitting during electrochemical measurements. The spectroelectrochemical behavior was confirmed by chemical oxidation of **Trux2** with the Co(III)-complex FK209 in dichloromethane (Figure S13).

In the case of Spiro-OMeTAD, the absorption spectral changes during electrochemical oxidation are completely different with respect to those observed for **Trux1** and **Trux2** (Figure 4C). In the first one-electron oxidation step (single oxidation; the potential was gradually increased from +0.50 to +0.64 V vs Ag/Ag^+), the UV-centered absorption band at 380 nm of the neutral molecule significantly decreased and typical strong visible/NIR absorptions of the corresponding Spiro-$OMeTAD^+$ appeared. The strong absorption band peaked at 522 nm can be ascribed to fluorene$^+$-localized transitions, while the absorption peaked at 687 nm attributable to N^+-localized transitions is barely detectable (Figure S14 and Table S3). Furthermore, during the potential increase up to +0.64 V, a strong absorption attributed to IVCT transition appeared as a broad band centered at ∼1545 nm. The observed behavior during the oxidative scan also proceeded in the course of the second oxidation event (single oxidation; the potential was gradually increased from +0.64 to +0.81 V vs Ag/Ag^+) and can be explained by the fact that the electron removal required for the formation of Spiro-$OMeTAD^{2+}$ involves the bis(*p*-anisyl)-amine subunits belonging to the other half of the molecule.

More importantly, the spectroelectrochemical results provide an explanation for the previously described electrochemical splitting of the oxidation events involving two noninteracting identical parts of the ground state molecule. It can rationally be explained by the instantaneous electron spin density delocalization along the whole molecule immediately following the formation of Spiro-$OMeTAD^+$ by 3-D homoconjugation, a hypothesis also corroborated by the theoretical investigations detailed below. In the course of the third two-electron oxidation step (double oxidation; the potential was gradually increased from +0.81 to +0.96 V vs Ag/Ag^+), a strong absorption peaked at 881 nm attributable to fluorene → N^+ charge transfer transitions readily appeared, accompanied by the progressive disappearance of the IVCT band. The occurrence of more pronounced N^+-localized (656 nm) and fluorene → N^+ charge transfer transitions suggests that the

DOI: 10.1021/acsami.7b05484
ACS Appl. Mater. Interfaces 2017, 9, 24778−24787

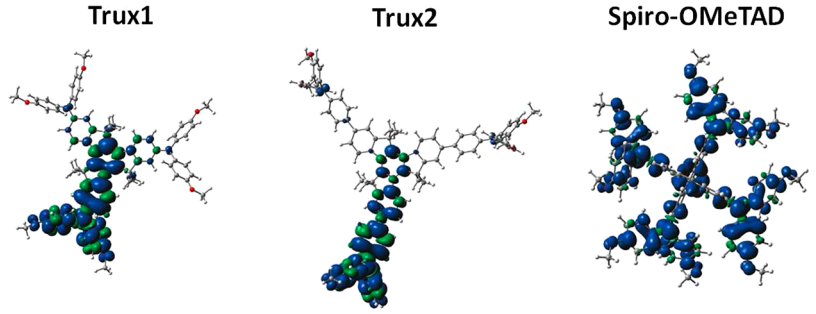

Figure 5. DFT-calculated electron spin density distributions (isovalue = 0.03 e/bohr^3) of **Trux1**$^{\bullet+}$, **Trux2**$^{\bullet+}$, and Spiro-OMeTAD$^{\bullet+}$ in the doublet state at the UCAMB3LYP/6-31G(d,p) level of theory.

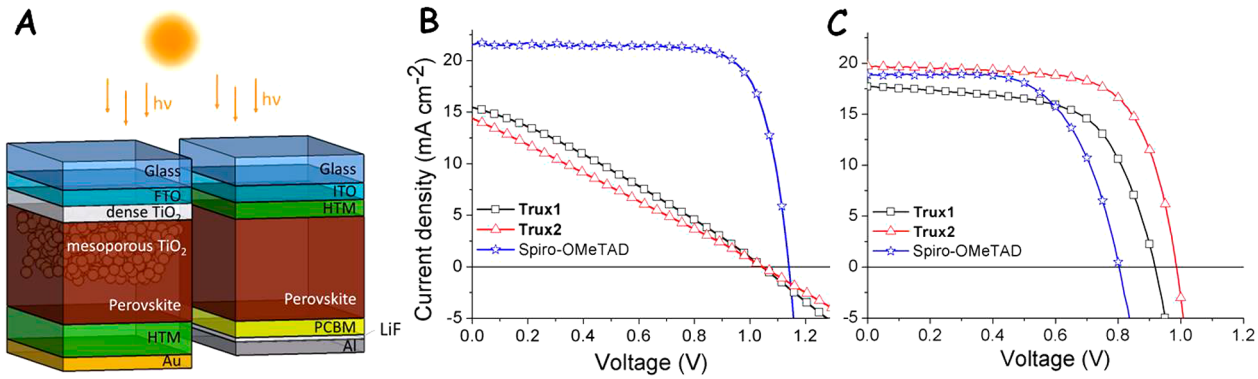

Figure 6. Schematic representation of n-i-p (left) and p-i-n (right) configuration devices (A) and current density−voltage (J−V) curves for a perovskite solar cells prepared with **Trux1**, **Trux2**, and Spiro-OMeTAD as HTMs in direct (B) or inverted (C) configuration devices.

Table 1. Photovoltaic Parameters for Trux1, Trux2, and Spiro-OMeTAD in the Different Configuration (n-i-p or p-i-n) Devices: Open-Circuit Voltage (V_{OC}), Short-Circuit Current (J_{SC}), Fill Factor (FF), and Power Conversion Efficiency (PCE)

HTM	device configuration	FF (%)	V_{OC} (V)	J_{SC} (mA/cm^2)	PCE (%)
Trux1	n-i-p	29	1.044	15.5	4.9
	p-i-n	63	0.918	17.7	10.2
Trux2	n-i-p	26	1.046	14.4	4.0
	p-i-n	69	0.986	19.7	13.4
Spiro-OMeTAD	n-i-p	76	1.141	21.5	19.2
	p-i-n	63	0.804	18.9	9.5

electron spin density in Spiro-OMeTAD^{3+} and Spiro-OMeTAD^{4+} is dominated by the bis(*p*-anisyl)amine subunits. Also in the case of Spiro-OMeTAD, the spectroelectrochemical behavior was mirrored by chemical oxidation with the Co(III)-complex FK209 in dichloromethane (Figure S15).

To rationalize the absorptions of the synthesized compounds in their radical cation states, electron spin density distributions were calculated on the DFT-optimized structures of the open-shell compounds. Suitable models were obtained by replacing the *n*-hexyl chains of **Trux1** and **Trux2** with methyl groups to reduce the calculation load. The results (Figure 5) are in line with the experimental observation concerning the presence and form of the low-energy broad band appearing in the course of the spectroelectrochemical measurements upon one-electron oxidation of **Trux1**, being the spin distribution not homogeneously delocalized between the three bis(*p*-anisyl)amine subunits. The calculated spin distribution in **Trux2**$^+$ is prevalently localized on one branch of the molecule, explaining the absence of the IVCT band upon one-electron oxidation. In the case of Spiro-OMeTAD, the electron spin density distribution involves the two sides of the molecule, substantiating the experimental observation of the electrochemical splitting.

Photovoltaic Properties. To test the properties of **Trux1** and **Trux2** as hole-transporting materials in PSCs, two different configuration devices were used and the results compared with those obtained using Spiro-OMeTAD as reference HTM. The J−V curves of the best performing PSC devices are reported in Figure 6, while the corresponding photovoltaic performance parameters, namely, short-circuit current density (J_{SC}), open-circuit voltage (V_{OC}), fill factor (FF), and PCE are listed in Table 1.

In their n-i-p configuration, devices based on **Trux1** and **Trux2** significantly underperform compared to the Spiro-OMeTAD. In particular, the J−V behavior appears like a strain line with respect to the diode-like curve shown by the Spiro-OMeTAD device, suggesting that the charge collection is strongly limited by series resistance.[48] It can be concluded that the **Trux1** and **Trux2** HTM layer in this configuration is significantly less conductive than the Spiro-OMeTAD one. We tried to reduce the series resistance by lowering the concentration of the HTM solution to generate a thinner HTM film. However, our attempt failed due to the roughness

DOI: 10.1021/acsami.7b05484
ACS Appl. Mater. Interfaces 2017, 9, 24778−24787

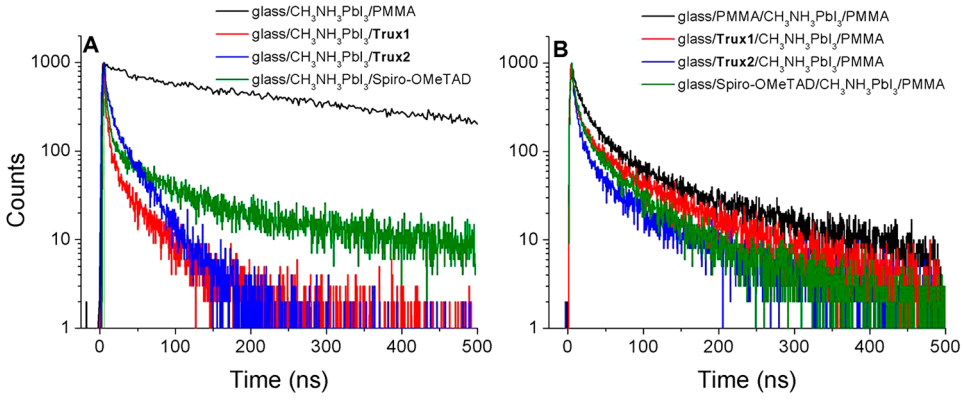

Figure 7. Time-resolved photoluminescence measurements of direct configuration devices (A) and inverted configuration devices (B). The decays are collected at the maximum of the perovskite emission band (780 nm).

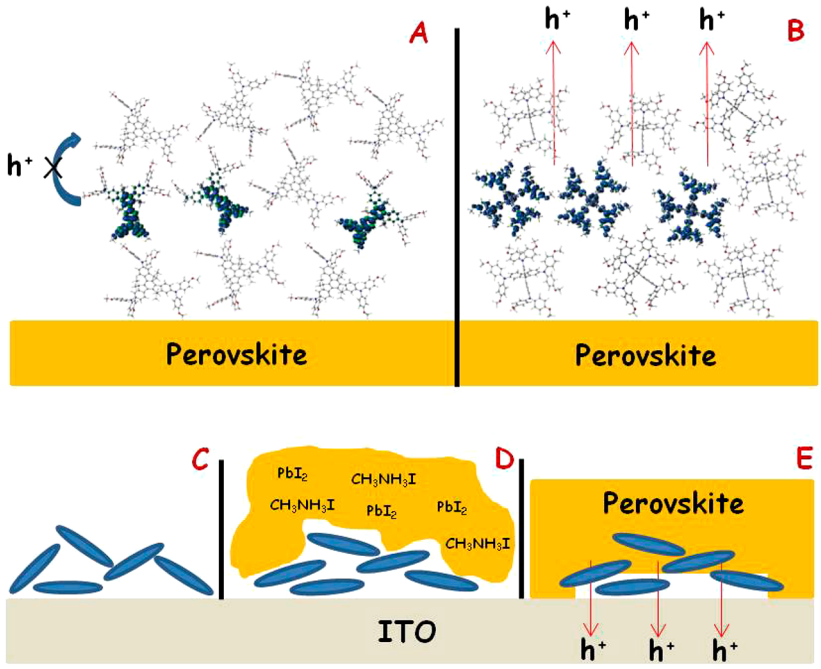

Figure 8. Top: pictorial representation of the alleged situation upon hole extraction at the perovskite/HTM interface for **Trux1** (A) and Spiro-OMeTAD (B) in direct configuration devices. Bottom: pictorial representation of the molecular arrangement of truxene-based molecules (blue disks) after deposition onto ITO (C), in contact with the solution of perovskite precursors (D) and following the perovskite growth (E) in p-i-n configuration devices.

of the perovskite surface inducing electric shunt pathways in the HTM films obtained from solution at a concentration below the optimized value used for the Spiro-OMeTAD. To overcome this issue, we fabricated inverted configuration (p-i-n) devices that allowed us to work with a significantly thinner HTM layer.

In the case of the inverted device configuration, both **Trux1** and **Trux2** achieved remarkable efficiencies, 10.2% and 13.4%, respectively, overcoming the 9.5% efficiency reached by the Spiro-OMeTAD reference in the analogous device configuration. These performances were achieved without the use of any dopant additive, confirming that the two molecules are prone to efficiently extract holes from the perovskite active layer. Full hysteresis scans are given in the Supporting Information (Figures S16 and S17 and Table S4).

To gain insight into the dynamics of hole transfer at the perovskite/HTM interface, we performed time-resolved photoluminescence decay measurements. The analysis was carried out on both configurations: the direct one in which the HTM has been deposited on top of the perovskite active layer and on the indirect one in which the perovskite was deposited on the hole-transporting layer. The behavior of **Trux1** and **Trux2** was compared with the Spiro-OMeTAD reference. To provide suitable reference for both configurations, the perovskite was deposited on glass and on PMMA (Figure 7).

The perovskite grown on the organic layer (PMMA) shows worse optical performances if compared with the one deposited on glass, as the latter exhibits very long PL decays, indicating low electronic trap densities and balanced carriers transport.[49,50] The role of the substrate in driving the growth of halide perovskite is fundamental for the performances of the material, as it influences nucleation and growth processes, structural order of the material, and grain size/shape distribution. From the measurements, it appears that PMMA is not an ideal growing substrate for the perovskite, and probably is not an ideal reference for our systems, embedding

DOI: 10.1021/acsami.7b05484
ACS Appl. Mater. Interfaces 2017, 9, 24778−24787

the active interface in the inverted configuration as PMMA differs from the HTMs for the absence of polar groups, likely increasing the substrate wettability toward the polar perovskite solvent precursor. Bearing this in mind, it is evident that there is a strong quenching of the perovskite excited state when all the three HTMs are screened in the two configurations. In the direct configuration, **Trux1** and **Trux2** seem to perform even better than Spiro-OMeTAD (Table S5). By contrast, in the inverted configuration, the three HTMs perform similarly with a slightly higher quenching rate observed for **Trux2** well mirroring the device performances. We can conclude that **Trux1** and **Trux2** can effectively act as hole extracting materials independently of device configurations. Therefore, other phenomena must be considered to explain the peculiar behavior of **Trux1** and **Trux2** in different configuration devices with respect to Spiro-OMeTAD.

Actually, in direct configurations, a HTM film (150−200 nm) is deposited onto the perovskite active layer, whereas, in inverted devices, a very thin film (5−20 nm) of HTM is layered directly on ITO, before the perovskite growth. We can suppose that, in the case of the n-i-p devices, where a thicker layer is required, a certain limitation to the transport properties of the HTM film takes place, leading to a disequilibrium between generated/extracted/transported charges at the perovskite/HTM interface. The localized electron spin densities calculated for **Trux1** and **Trux2** in their radical cation state can be accounted for being an obstacle to the smooth hole hopping (following the interfacial hole extraction from perovskite) by reducing the likelihood of HTM/HTM$^+$ active contacts through their bis(*p*-anisyl)amine subunits, and this situation is exacerbated by the presence of flexible alkyl chains (Figure 8A) deliberately added to warrant solubility. The effect of alkyl chains decorating the HTM scaffold on the PSC performances in n-i-p configurations was recently scrutinized by Nazeeruddin and co-workers[51] as well as by Hagfeldt and co-workers:[52] while the charge extraction and hole mobility are negatively affected by peripherally positioning the alkyl chains, the effect is indeed beneficial when they are placed in proximity of the core.

Conversely, the unsurpassed hole-transporting properties of the popular referential HTM in inorganic/organic heterojunctions seem to be ascribable to the 3-D electron spin density distribution in its radical cation state, ensuring a regular intermolecular hole hopping through the active contacts between the molecules (Figure 8B). This is underlined in our work by the peculiarities emerged comparing the direct configuration device layouts. Nevertheless, when the perovskite absorber is assembled onto a very thin organic layer, **Trux1** and **Trux2** outperform the Spiro-OMeTAD reference. We believe that, during the p-i-n device construction, the contact between the organic layer of **Trux1** and **Trux2** and the polar solvent[53] dissolving the perovskite precursors, followed by the thermal treatment required for the perovskite layer generation, can reasonably promote the formation of a favorable molecular arrangement at the perovskite/HTM interface (Figure 8C−E), ensuring efficient device performances in spite of the intrinsic charge transport properties of the employed HTMs.

CONCLUSIONS

The performances of new hole-transporting materials were investigated for the first time in perovskite-based solar cells intentionally assembled into two different (direct and inverted) architectures, and compared with those of the state-of-the-art 2,2′,7,7′-tetrakis(*N*,*N*-di-*p*-methoxyphenylamine)-9,9′-spirobifluorene (Spiro-OMeTAD) reference. Star-shaped hole-transporting materials were designed by binding the bis(*p*-methoxyphenyl)amine groups to a truxene-based core (**Trux1**) and by interspacing these electron-donating functionalities from the core with 1,4-phenylene π-bridges (**Trux2**). We suppose that photovoltaic responses of the two molecules, dramatically different when employed in direct or inverted configuration PSCs, depend on intramolecular charge distributions in radical cations, combined with the thickness of the HTM layers. Since photoluminescence decay measurements suggested an even better hole extraction from the perovskite absorbing layer in direct configuration devices with respect to Spiro-OMeTAD (which exhibited efficiencies up to 19.2%), the performances of **Trux1** and **Trux2** (4−5%) were heavily influenced by the reduced hole-transport properties, likely ascribable to the mandatorily thicker HTM layer. The results of our investigations indicate the 3-D charge distribution of Spiro-OMeTAD radical cation as the cause of the excellent behavior of this HTM reference, favoring a smooth hole transport across adjacent molecules. On the other hand, the trend of the photovoltaic response observed for the p-i-n architecture devices was completely reversed: since, in this configuration, the use of a very thin HTM layer was allowed and the perovskite absorber was assembled onto the organic layer, a more favorable perovskite/HTM interface was generated due to the tailored 2-D structure of the truxene-based HTMs, boosting the performances of **Trux2** up to 13.4% compared to the 9.5% of the Spiro-OMeTAD reference device. We believe that understanding the HTM role in differently configured PSCs could open new frontiers for the rational manipulation of the perovskite/HTM interface aiming at improving performances beyond the state-of-the-art.

ASSOCIATED CONTENT

Supporting Information

The Supporting Information is available free of charge on the ACS Publications website at DOI: 10.1021/acsami.7b05484.

Synthetic details and methods. Additional characterization of compounds and devices (PDF)

AUTHOR INFORMATION

Corresponding Authors

*E-mail: roberto.grisorio@poliba.it (R.G.).
*E-mail: luisa.demarco@nanotec.cnr.it (L.D.M.).
*E-mail: antonio.abate@helmholtz-berlin.de (A.A.).

ORCID

Roberto Grisorio: 0000-0002-3698-9370
Michele Manca: 0000-0002-6903-2954
Antonio Abate: 0000-0002-3012-3541

Notes

The authors declare no competing financial interest.

ACKNOWLEDGMENTS

The authors gratefully acknowledge the following funding sources. The Austrian Research Promotion Agency-FFG (Bridge-Early Stage COMPOSTRONICS cod. 5730587). Italian MIUR PON2 "Molecular NAnotechnology for HeAlth and EnvironmenT" (MAAT cod. PON02_00563_3316357 - CUP B31C12001230005). Italian MIUR SIR "Two-Dimensional Colloidal Metal Dichalcogenides based Energy-Conversion Photovoltaics" (2D ECO cod. RBSI14-FYVD) DD 197,

DOI: 10.1021/acsami.7b05484
ACS Appl. Mater. Interfaces 2017, 9, 24778−24787

23/01/14. Italian MIUR PRIN 2015 - "PERrovskite-based Solar cells: towards high Efficiency and long-term stability" (PERSEO cod. 20155LECAJ) DD 2488, 4/11/15. The Adolphe Merkle and the Swiss National Science Foundation (Program NRP70 No. 153990). The Apulia Region project "NANOAPULIA- nanofotocatalizzatori per un'atmosfera più pulita" (Cluster Tecnologici Regionali cod. MDI6SR1 - CUP B38C14001140008). Apulia Region and ARTI for Future in Research project "HyLight" no. GOWMB21.

REFERENCES

(1) Tao, Y.; Yang, C.; Qin, J. Organic Host materials for Phosphorescent Organic Light-emitting Diodes. *Chem. Soc. Rev.* **2011**, *40*, 2943−2970.
(2) Calió, L.; Kazim, S.; Grätzel, M.; Ahmad, S. Hole-Transport Materials for Perovskite Solar Cells. *Angew. Chem., Int. Ed.* **2016**, *55*, 14522−14545.
(3) Yan, W.; Ye, S.; Li, Y.; Sun, W.; Rao, H.; Liu, Z.; Bian, Z.; Huang, C. Hole-Transporting Materials in Inverted Planar Perovskite Solar Cells. *Adv. Energy Mater.* **2016**, *6*, 1600474.
(4) Liu, T.; Chen, C.; Hu, Q.; Zhu, R.; Gong, Q. Inverted Perovskite Solar Cells: Progresses and Perspectives. *Adv. Energy Mater.* **2016**, *6*, 1600457.
(5) Stranks, S. D.; Nayak, P. K.; Zhang, W.; Stergiopoulos, T.; Snaith, H. J. Formation of Thin Films of Organic−Inorganic Perovskites for High-Efficiency Solar Cells. *Angew. Chem., Int. Ed.* **2015**, *54*, 3240−3248.
(6) Burschka, J.; Pellet, N.; Moon, S. J.; Humphry-Baker, R.; Gao, P.; Nazeeruddin, M. K.; Graetzel, M. Sequential Deposition as a Route to High-performance Perovskite-sensitized Solar Cells. *Nature* **2013**, *499*, 316−319.
(7) Liu, M.; Johnston, M. B.; Snaith, H. J. Efficient Planar Heterojunction Perovskite Solar Cells by Vapour Deposition. *Nature* **2013**, *501*, 395−398.
(8) Lee, M. M.; Teuscher, J.; Miyasaka, T.; Murakami, T. N.; Snaith, H. J. Efficient Hybrid Solar Cells Based on Meso-Superstructured Organometal Halide Perovskites. *Science* **2012**, *338*, 643−647.
(9) Kojima, A.; Teshima, K.; Shirai, Y.; Miyasaka, T. Organometal Halide Perovskites as Visible-Light Sensitizers for Photovoltaic Cells. *J. Am. Chem. Soc.* **2009**, *131*, 6050−6051.
(10) Xu, B.; Bi, D.; Hua, Y.; Liu, P.; Cheng, M.; Graetzel, M.; Kloo, L.; Hagfeldt, A.; Sun, L. A Low-cost Spiro[fluorene-9,9′-xanthene]-based Hole Transport Material for Highly Efficient Solid-state Dye-sensitized Solar Cells and Perovskite Solar Cells. *Energy Environ. Sci.* **2016**, *9*, 873−877.
(11) Hua, Y.; Zhang, J.; Xu, B.; Liu, P.; Cheng, M.; Kloo, L.; Johansson, E. M. J.; Sveinbjörnsson, K.; Aitola, K.; Boschloo, G.; Sun, L. Facile Synthesis of Fluorene-based Hole Transport Materials for Highly Efficient Perovskite Solar Cells and Solid-state Dye-sensitized Solar Cells. *Nano Energy* **2016**, *26*, 108−113.
(12) Saliba, M.; Orlandi, S.; Matsui, T.; Aghazada, S.; Cavazzini, M.; Correa-Baena, J. P.; Gao, P.; Scopelliti, R.; Mosconi, E.; Dahmen, K. H.; De Angelis, F.; Abate, A.; Hagfeldt, A.; Pozzi, G.; Graetzel, M.; Nazeeruddin, M. K. A Molecularly Engineered Hole-transporting Material for Efficient Perovskite Solar Cells. *Nat. Energy* **2016**, *1*, 15017.
(13) Malinauskas, T.; Saliba, M.; Matsui, T.; Daskeviciene, M.; Urnikaite, S.; Gratia, P.; Send, R.; Wonneberger, H.; Bruder, I.; Graetzel, M.; Getautis, V.; Nazeeruddin, M. K. Branched Methoxydiphenylamine-substituted Fluorene Derivatives as Hole Transporting Materials for High-performance Perovskite Solar Cells. *Energy Environ. Sci.* **2016**, *9*, 1681−1686.
(14) Rakstys, K.; Saliba, M.; Gao, P.; Gratia, P.; Kamarauskas, E.; Paek, S.; Jankauskas, V.; Nazeeruddin, M. K. Highly Efficient Perovskite Solar Cells Employing an Easily Attainable Bifluorenylidene-Based Hole-Transporting Material. *Angew. Chem., Int. Ed.* **2016**, *55*, 7464−7468.
(15) Zhang, J.; Hua, Y.; Xu, B.; Yang, L.; Liu, P.; Johansson, M. B.; Vlachopoulos, N.; Kloo, L.; Boschloo, G.; Johansson, E. M. J.; Sun, L.; Hagfeldt, A. The Role of 3D Molecular Structural Control in New Hole Transport Materials Outperforming Spiro-OMeTAD in Perovskite Solar Cells. *Adv. Energy Mater.* **2016**, *6*, 1601062.
(16) Bi, D.; Xu, B.; Gao, P.; Sun, L.; Grätzel, M.; Hagfeldt, A. Facile Synthesized Organic Hole Transporting Material for Perovskite Solar Cell with Efficiency of 19.8%. *Nano Energy* **2016**, *23*, 138−144.
(17) Zhang, J.; Xu, B.; Johansson, M. B.; Vlachopoulos, N.; Boschloo, G.; Sun, L.; Johansson, E. M. J.; Hagfeldt, A. Strategy to Boost the Efficiency of Mixed-Ion Perovskite Solar Cells: Changing Geometry of the Hole Transporting Material. *ACS Nano* **2016**, *10*, 6816−6825.
(18) Gratia, P.; Magomedov, A.; Malinauskas, T.; Daskeviciene, M.; Abate, A.; Ahmad, S.; Graetzel, M.; Getautis, V.; Nazeeruddin, M. K. A Methoxydiphenylamine-Substituted Carbazole Twin Derivative: An Efficient Hole-Transporting Material for Perovskite Solar Cells. *Angew. Chem., Int. Ed.* **2015**, *54*, 11409−11413.
(19) Rakstys, K.; Abate, A.; Dar, M. I.; Gao, P.; Jankauskas, V.; Jacopin, G.; Kamarauskas, E.; Kazim, S.; Ahmad, S.; Grätzel, M.; Nazeeruddin, M. K. Triazatruxene-Based Hole Transporting Materials for Highly Efficient Perovskite Solar Cells. *J. Am. Chem. Soc.* **2015**, *137*, 16172−16178.
(20) Cho, K. T.; Trukhina, O.; Roldán-Carmona, C.; Ince, M.; Gratia, P.; Grancini, G.; Gao, P.; Marszalek, T.; Pisula, W.; Reddy, P. Y.; Torres, T.; Nazeeruddin, M. K. Molecularly Engineered Phthalocyanines as Hole-Transporting Materials in Perovskite Solar Cells Reaching Power Conversion Efficiency of 17.5%. *Adv. Energy Mater.* **2017**, *7*, 1601733.
(21) Paek, S.; Zimmermann, I.; Gao, P.; Gratia, P.; Rakstys, K.; Grancini, G.; Nazeeruddin, M. K.; Rub, M. A.; Kosa, S. A.; Alamry, K. A.; Asiri, A. M. Donor−π−donor Type Hole Transporting Materials: Marked π-Bridge Effects on Optoelectronic Properties, Solid-state Structure, and Perovskite Solar Cell Efficiency. *Chem. Sci.* **2016**, *7*, 6068−6075.
(22) Cheng, M.; Chen, C.; Yang, X.; Huang, J.; Zhang, F.; Xu, B.; Sun, L. Novel Small Molecular Materials Based on Phenoxazine Core Unit for Efficient Bulk Heterojunction Organic Solar Cells and Perovskite Solar Cells. *Chem. Mater.* **2015**, *27*, 1808−1814.
(23) Kazim, S.; Ramos, F. J.; Gao, P.; Nazeeruddin, M. K.; Graetzel, M.; Ahmad, S. A Dopant Free Linear Acene Derivative as a Hole Transport Material for Perovskite Pigmented Solar Cells. *Energy Environ. Sci.* **2015**, *8*, 1816−1823.
(24) Steck, C.; Franckevicius, M.; Zakeeruddin, S. M.; Mishra, A.; Bauerle, P.; Gratzel, M. A−D−A-type S,N-Heteropentacene-based Hole Transport Materials for Dopant-free Perovskite Solar Cells. *J. Mater. Chem. A* **2015**, *3*, 17738−17746.
(25) Liu, Y.; Chen, Q.; Duan, H. S.; Zhou, H.; Yang, Y.; Chen, H.; Luo, S.; Song, T. B.; Dou, L.; Hong, Z.; Yang, Y. A Dopant-free Organic Hole Transport Material for Efficient Planar Heterojunction Perovskite Solar Cells. *J. Mater. Chem. A* **2015**, *3*, 11940−11947.
(26) Do, K.; Choi, H.; Lim, K.; Jo, H.; Cho, J. W.; Nazeeruddin, M. K.; Ko, J. Star-Shaped Hole Transporting Materials with a Triazine Unit for Efficient Perovskite Solar Cells. *Chem. Commun.* **2014**, *50*, 10971−10974.
(27) Krishnamoorthy, T.; Kunwu, F.; Boix, P. P.; Li, H.; Koh, T. M.; Leong, W. L.; Powar, S.; Grimsdale, A.; Graetzel, M.; Mathews, N.; Mhaisalkar, S. G. A Swivel-Cruciform Thiophene Based Hole-Transporting Material for Efficient Perovskite Solar Cells. *J. Mater. Chem. A* **2014**, *2*, 6305−6309.
(28) Li, H.; Fu, K.; Hagfeldt, A.; Graetzel, M.; Mhaisalkar, S. G.; Grimsdale, A. C. A Simple 3,4-Ethylenedioxythiophene Based Hole-Transporting Material for Perovskite Solar Cells. *Angew. Chem., Int. Ed.* **2014**, *53*, 4085−4088.
(29) Lim, I.; Kim, E.-K.; Patil, S. A.; Ahn, D. Y.; Lee, W.; Shrestha, N. K.; Lee, J. K.; Seok, W. K.; Cho, C.-G.; Han, S.-H. Indolocarbazole Based Small Molecules: an Efficient Hole Transporting Material for Perovskite Solar Cells. *RSC Adv.* **2015**, *5*, 55321−55327.
(30) Goubard, F.; Dumur, F. Truxene: a Promising Scaffold for Future Materials. *RSC Adv.* **2015**, *5*, 3521−3551.

DOI: 10.1021/acsami.7b05484
ACS Appl. Mater. Interfaces 2017, 9, 24778−24787

(31) In the course of our studies, this molecule has been applied in optimized inverted PSCs employing a different electron-transporting layer with respect to the one here reported: Huang, C.; Fu, W.; Li, C.-Z.; Zhang, Z.; Qiu, W.; Shi, M.; Heremans, P.; Jen, A. K.-Y.; Chen, H. Dopant-Free Hole-Transporting Material with a C_{3h} Symmetrical Truxene Core for Highly Efficient Perovskite Solar Cells. *J. Am. Chem. Soc.* **2016**, *138*, 2528−2531.
(32) Hu, Z.; Fu, W.; Yan, L.; Miao, J.; Yu, H.; He, Y.; Goto, O.; Meng, H.; Chen, H.; Huang, W. Effects of Heteroatom Substitution in Spiro-bifluorene Hole Transport Materials. *Chem. Sci.* **2016**, *7*, 5007−5012.
(33) Kanibolotsky, A. L.; Berridge, R.; Skabara, P. J.; Perepichka, I. F.; Bradley, D. D. C.; Koeberg, M. Synthesis and Properties of Monodisperse Oligofluorene-Functionalized Truxenes: Highly Fluorescent Star-Shaped Architectures. *J. Am. Chem. Soc.* **2004**, *126*, 13695−13702.
(34) Grisorio, R.; Roose, B.; Colella, S.; Listorti, A.; Suranna, G. P.; Abate, A. Molecular Tailoring of Phenothiazine-Based Hole-Transporting Materials for Highly Performing Perovskite Solar Cells. *ACS Energy Lett.* **2017**, *2*, 1029−1034.
(35) Abate, A.; Paek, S.; Giordano, F.; Correa-Baena, J.-P.; Saliba, M.; Gao, P.; Matsui, T.; Ko, J.; Zakeeruddin, S. M.; Dahmen, K. H.; Hagfeldt, A.; Graetzel, M.; Nazeeruddin, M. K. Silolothiophene-Linked Triphenylamines as Stable Hole Transporting Materials for High Efficiency Perovskite Solar Cells. *Energy Environ. Sci.* **2015**, *8*, 2946−2953.
(36) Malinauskas, T.; Tomkute-Luksiene, D.; Sens, R.; Daskeviciene, M.; Send, R.; Wonneberger, H.; Jankauskas, V.; Bruder, I.; Getautis, V. Enhancing Thermal Stability and Lifetime of Solid-State Dye-Sensitized Solar Cells via Molecular Engineering of the Hole-Transporting Material Spiro-OMeTAD. *ACS Appl. Mater. Interfaces* **2015**, *7*, 11107−11116.
(37) Heckmann, A.; Lambert, C. Organic Mixed-Valence Compounds: a Playground for Electrons and Holes. *Angew. Chem., Int. Ed.* **2012**, *51*, 326−392.
(38) Hankache, J.; Wenger, O. S. Organic Mixed Valence. *Chem. Rev.* **2011**, *111*, 5138−5178.
(39) Winter, R. F. Half-Wave Potential Splittings ΔE1/2 as a Measure of Electronic Coupling in Mixed-Valent Systems: Triumphs and Defeats. *Organometallics* **2014**, *33*, 4517−4536.
(40) Kaafarani, B. R.; Risko, C.; El-Assaad, T. H.; El-Ballouli, A. O.; Marder, S. R.; Barlow, S. Mixed-Valence Cations of Di(carbazol-9-yl) Biphenyl, Tetrahydropyrene, and Pyrene Derivatives. *J. Phys. Chem. C* **2016**, *120*, 3156−3166.
(41) Shen, J.-J.; Shao, J.-Y.; Zhu, X.; Zhong, Y.-W. Amine−Amine Electronic Coupling through a Dibenzo[a,e]pentalene Bridge. *Org. Lett.* **2016**, *18*, 256−259.
(42) Nie, H.-J.; Yao, C.-J.; Shao, J.-Y.; Yao, J.; Zhong, Y.-W. Oligotriarylamines with a Pyrene Core: A Multicenter Strategy for Enhancing Radical Cation and Dication Stability and Tuning Spin Distribution. *Chem. - Eur. J.* **2014**, *20*, 17454−17465.
(43) Nie, H.-J.; Chen, X.; Yao, C.-J.; Zhong, Y.-W.; Hutchison, G. R.; Yao, J. Electronic Coupling between Two Amine Redox Sites through the 5,5′-Positions of Metal-Chelating 2,2′-Bipyridines. *Chem. - Eur. J.* **2012**, *18*, 14497−15509.
(44) Barlow, S.; Risko, C.; Odom, S. A.; Zheng, S.; Coropceanu, V.; Beverina, L.; Bredas, J.-L.; Marder, S. R. Tuning Delocalization in the Radical Cations of 1,4-Bis[4-(diarylamino)styryl]benzenes, 2,5-Bis[4-(diarylamino)styryl]thiophenes, and 2,5-Bis[4-(diarylamino)styryl]-pyrroles through Substituent Effects. *J. Am. Chem. Soc.* **2012**, *134*, 10146−10155.
(45) Yan, Q.; Guo, Y.; Ichimura, A.; Tsuji, H.; Nakamura, E. Three-Dimensionally Homoconjugated Carbon-Bridged Oligophenylenevinylene for Perovskite Solar Cells. *J. Am. Chem. Soc.* **2016**, *138*, 10897−10904.
(46) Saliba, M.; Matsui, T.; Seo, J.-Y.; Domanski, K.; Correa-Baena, J.-P.; Nazeeruddin, M. K.; Zakeeruddin, S. M.; Tress, W.; Abate, A.; Hagfeldt, A.; Graetzel, M. Cesium-Containing Triple Cation Perovskite Solar Cells: Improved Stability, Reproducibility and High Efficiency. *Energy Environ. Sci.* **2016**, *9*, 1989−1997.
(47) Bredas, J.-L. Mind the Gap! *Mater. Horiz.* **2014**, *1*, 17−19.
(48) Ma, W.; Yang, C.; Gong, X.; Lee, K.; Heeger, A. J. Thermally Stable, Efficient Polymer Solar Cells with Nanoscale Control of the Interpenetrating Network Morphology. *Adv. Funct. Mater.* **2005**, *15*, 1617−1622.
(49) Colella, S.; Mazzeo, M.; Rizzo, A.; Gigli, G.; Listorti, A. The Bright Side of Perovskites. *J. Phys. Chem. Lett.* **2016**, *7*, 4322−4334.
(50) Grisorio, R.; Piliego, C.; Striccoli, M.; Cosma, P.; Fini, P.; Gigli, G.; Mastrorilli, P.; Suranna, G. P.; Nobile, C. F. Influence of Keto Groups on the Optical, Electronic, and Electroluminescent Properties of Random Fluorenone-Containing Poly(fluorenylene-vinylene)s. *J. Phys. Chem. C* **2008**, *112*, 20076−20087.
(51) Zimmermann, I.; Urieta-Mora, J.; Gratia, P.; Aragó, J.; Grancini, G.; Molina-Ontoria, A.; Ortí, E.; Martín, N.; Nazeeruddin, M. K. High-Efficiency Perovskite Solar Cells Using Molecularly Engineered, Thiophene-Rich, Hole-Transporting Materials: Influence of Alkyl Chain Length on Power Conversion Efficiency. *Adv. Energy Mater.* **2017**, *7*, 1601674.
(52) Zhang, J.; Xu, B.; Johansson, M. B.; Hadadian, M.; Correa Baena, J. P.; Liu, P.; Hua, Y.; Vlachopoulos, N.; Johansson, E. M. J.; Boschloo, G.; Sun, L.; Hagfeldt, A. Constructive Effects of Alkyl Chains: A Strategy to Design Simple and Non-Spiro Hole Transporting Materials for High-Efficiency Mixed-Ion Perovskite Solar Cells. *Adv. Energy Mater.* **2016**, *6*, 1502536.
(53) Khan, H. U.; Li, R.; Ren, Y.; Chen, L.; Payne, M. M.; Bhansali, U. S.; Smilgies, D.-M.; Anthony, J. E.; Amassian, A. Solvent Vapor Annealing in the Molecular Regime Drastically Improves Carrier Transport in Small-Molecule Thin-Film Transistors. *ACS Appl. Mater. Interfaces* **2013**, *5*, 2325−2330.

DOI: 10.1021/acsami.7b05484
ACS Appl. Mater. Interfaces 2017, 9, 24778−24787